European Journal of Organic Chemistry

EurJOC
European Journal of Organic Chemistry

Chemistry Europe
European Chemical Societies Publishing

RESEARCH ARTICLE OPEN ACCESS

Competing Charge Transport Pathways: A Spirobifluorene-Based Molecular Loop

Brian Ogi[1] | Riccardo Conte[2] | Salome L. Heim[1] | Herre S. J. van der Zant[2] | Marcel Mayor[1,3,4]

[1]Department of Chemistry, University of Basel, Basel, Switzerland | [2]Kavli Institute of Nanoscience, Delft University of Technology, Delft, The Netherlands | [3]Institute for Nanotechnology (INT), Karlsruhe Institute of Technology (KIT), Karlsruhe, Germany | [4]Lehn Institute of Functional Materials (LIFM), School of Chemistry, Sun Yat-Sen University (SYSU), Guangzhou, China

Correspondence: Herre S. J. van der Zant (H.S.J.vanderZant@tudelft.nl) | Marcel Mayor (marcel.mayor@chemie.unibas.ch)

Received: 10 June 2026 | **Revised:** 31 July 2026 | **Accepted:** 3 August 2026

Keywords: conductance pathways | cycloparaphenylene | mechanically controlled break junctions | spiroconjugation | strained macrocycle

ABSTRACT

Understanding the relationship between molecular structure and charge transport remains a crucial aspect towards integrating single molecules into electronic devices, especially in systems which feature multiple conducting pathways. Here we report the synthesis of a molecular loop that incorporates a rigid 9,9′-spirobifluorene (SBF) core as a central mounting point for thiol anchoring groups and a cycloparaphenylene (CPP) backbone. The model compound is synthesized by a Suzuki–Miyaura coupling between a CPP precursor and a functionalized SBF derivative, followed by reductive aromatization of the macrocycle. The resulting macrocycles are fully characterized and enantiomerically resolved by chiral high-performance liquid chromatography (HPLC), and their chiroptical properties are investigated. Conductance measurements in a mechanically controlled break-junction (MCBJ) setup demonstrate reproducible single-molecule junction formation with two dominant conductance plateaus near 2×10^{-4} G_0 and 4×10^{-5} G_0, observed across different samples and applied voltages. The observed conductance features are consistent with multiple reproducible junction configurations, highlighting the molecular loop as a promising platform for studying charge transport through multiple intramolecular pathways.

1 | Introduction

The ongoing miniaturization of electronic devices has driven intense research into the development of molecular-scale components capable of performing classical electronic functions [1]. Within this context, molecular electronics aim to exploit individual molecules as conductors, switches [2–4], or rectifiers/diodes [5–7] with the goal of integrating them into nanoscale circuits [8]. One prominent class of such systems are molecular wires, a single molecule that bridges two metallic electrodes and facilitates charge transport along a well-defined pathway [9, 10]. Since the first experimental demonstrations of current flow through single molecules in the 1990s [11], a wide range of π-conjugated systems have been explored for their ability to support coherent electron tunneling or hopping transport mechanisms [12–16]. These studies have not only deepened our understanding of charge delocalization and quantum interference at the molecular level, but also revealed that even subtle changes in molecular structure can have a significantly impact on conductance [17, 18]. Thus, the knowledge of the correlation between molecular structure and electron transport is crucial for the design of functional molecular electronic components.

While early charge transport studies have primarily focused on linear [19] or cross-conjugated molecules [20, 21], recent work has highlighted the role of quantum interference effects, particularly in systems with multiple conjugation pathways [22–24]. A structural motif that can give access to such dual pathway architectures is 9,9′-spirobifluorene (SBF), where two π-conjugated fluorene units are linked orthogonally via a central sp^3-hybridized

carbon atom. This orthogonal arrangement interrupts through-bond conjugation between the two aromatic planes, effectively creating an insulating subunit. Yang and coworkers demonstrated that molecular junctions featuring orthogonal spiro connectivity exhibit a pronounced reduction in conductance across the spiro node, compared to linear conjugated analogs [25]. However, this geometry allows for unique through-space orbital interaction, referred to as spiroconjugation [26] (Figure 1b), which has enabled the use of SBF-based frameworks as matrix materials in optoelectronic devices [27] like solar cells [28] or organic light-emitting diodes (OLEDs) [29] and also as rigid tripodal platforms in scanning tunneling microscopy (STM) based single molecule junctions [30, 31]. The unique, rigid X-shaped structure of the SBF lends itself to the formation of macrocyclic structures which have been studied for their chiroptical properties [32, 33] and as host-guest systems [34]. Notably, Jasti and coworkers reported a chiral figure-eight shaped macrocycle composed out of two cycloparaphenylene (CPP) segments linked through a central SBF unit, highlighting its unique topology and chiroptical properties [35]. While CPPs are commonly studied in the context of armchair carbon nanotubes (CNTs) [36–38], their electronic properties have more recently been investigated in single-molecule junctions [39–41]. STM-break junction studies of [*n*]CPPs revealed that their radial π-conjugation (Figure 1c) results in significantly higher conductance compared to their linear analogs, with conductance increasing as ring size decreases due to an enhanced orbital overlap [40].

Thus far, systems that integrate orthogonal and radial conjugation pathways within a single rigid macrocyclic framework remain largely unexplored in the context of charge transport. Here the synthesis together with preliminary charge transport measurements of a compact molecular loop architecture combining an SBF core with a curved CPP subunit is reported. As sketched in Figure 1a, the macrocyclic model compound features two distinct electronic pathways: one across the orthogonal fluorene units via spiro-conjugation (sketched in green) and one along the radial π-conjugation of the CPP backbone (sketched in orange). While neither pathway individually ensures efficient conductance, their coexistence within a rigid, nonplanar π-system enables the investigation of topological and geometric effects on charge transport. This study highlights the synthetic accessibility of the macrocyclic scaffold and establishes it as a new platform to study pathway-dependent conductance features together with potentially emerging interference phenomena.

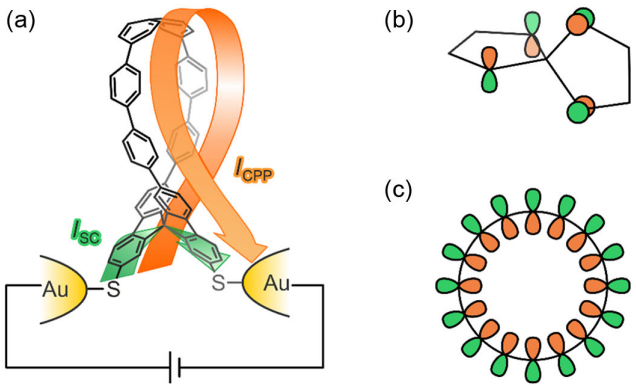

FIGURE 1 | (a) Concept drawing of the molecular junction consisting of the SBF-based molecular loop immobilized in between two gold electrodes. The two conductance pathways are highlighted by colored arrows from the left to the right. While the spiro-conjugated pathway (I_{SC}) is given with a green arrow on the molecular structure, the current pathway through the loop (I_{CPP}) is indicated by an orange arrow, which is offset to the right to increase the visibility of the drawing. (b) Illustration of the neighboring *p*-orbitals involved in spiro-conjugation by trough-space interactions. (c) Sketch of the radial *p*-orbital arrangement in a CPP.

2 | Results and Discussion

2.1 | Design and Retrosynthesis

The molecular design is displayed in Figure 1a. The molecular architecture consists of a rigid 9,9′-SBF scaffold, which serves as a central core unit for both the thiol anchoring groups and the CPP backbone. While the SBF subunit not only guarantees structural integrity, it also bends the molecular wire into a helical chiral arrangement. The macrocyclic architecture gives rise to two distinct transport channels, both with special conjugation features. The shorter connection through the central sp^3 hybridized C-atom of the SBF core can be described as spiro-conjugation (Figure 1a, green arrow, I_{SC}), relying on through-space *p*-orbital overlap between the orthogonally oriented fluorene moieties (Figure 1b). In the longer pathway through the loop (Figure 1a, orange arrow, I_{CPP}), the CPP fragments extend the linear conjugation of the sp^2-hybridized C-atoms of the fluorenes' biphenyl motive by radial π-conjugation (Figure 1c). Although the CPP path is relatively long, the macrocyclic strain enforces a radial orientation of the phenylene rings and compresses their π-system inwards, thereby enhancing orbital overlap and promoting efficient charge delocalization. The coexistence of both transport channels is not only of interest to study structural-dependent conductance in molecular junctions but also holds the potential of interference phenomena.

The synthetic strategy towards the target structure **1** is displayed in Scheme 1. Given the well-established synthesis protocols for CPPs, a macrocyclization between a functionalized SBF unit **4** and a [6]CPP precursor (**3**) was favored over a sequential build-up from the SBF core. The CPP precursor design follows established strategies based on protected 1,4-dihydroxycyclo-hexa-2,5-dienes as corner units. While triethylsilyl (TES) ethers are often employed due to their high stereoselectivity and thus improved yields [42, 43], methoxy groups were selected here for their synthetic simplicity and chemical stability. This choice is further justified by the absence of functional groups, sensitive to harsh conditions typically associated with the reductive aromatization step. Thiol functional groups were introduced at the SBF core prior to macrocyclization, as postfunctionalization was expected to be sterically challenging due to the rigid and congested environment. For compatibility with single-molecule break-junction experiments, the thiols were masked as acetyl protected derivatives, which undergo mild deprotection to form efficient gold–sulfur contacts. However, due to the limited stability of S-acetyl groups under standard basic conditions, the more robust ethyltrimethylsilyl (ethyl–TMS) group was used during the synthetic sequence. Ethyl–TMS offers a significant offset in polarity, enhances

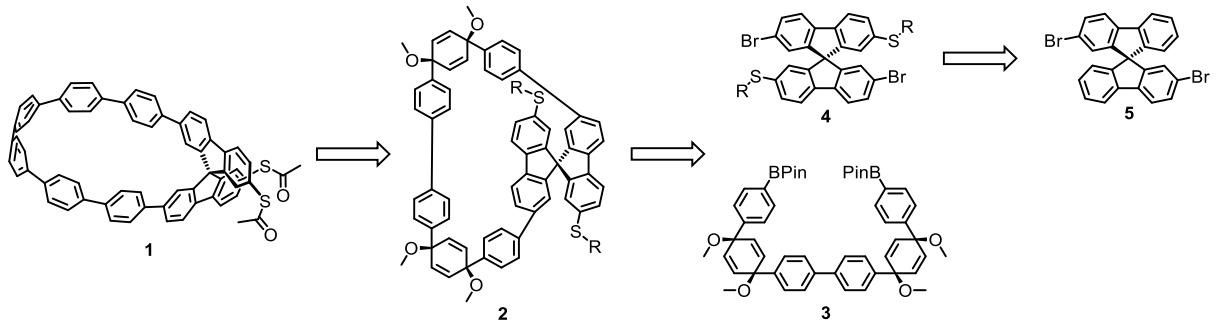

SCHEME 1 | Retrosynthetic analysis of the molecular loop **1**. (R = $(CH_2)_2$-TMS).

solubility of the otherwise poorly soluble SBF derivatives, and allows for selective, mild deprotection with fluoride sources, facilitating both macrocyclization and purification.

The final transformation involves a late stage transprotection of the ethyl-TMS masked thiol to the corresponding acetyl protected sulfur group. The fully aromatized molecular wire is obtained from the partially saturated precursor **2** via tin-mediated reductive aromatization, following well-established protocols for CPP-based systems [42]. The macrocycle **2** is assembled through a Suzuki–Miyaura cross-coupling between the borylated [6]CPP precursor **3** and the functionalized SBF **4**. Precursor **3** is well established in literature [44] and can be accessible in a few synthetic steps from commercially available 4-bromo-4′-hydroxybiphenyl. The SBF **4** is derived from commercially available 2,2′-dibromo-9,9′-SBF (**5**) via regioselective di-iodination at the 7,7′-positions, followed by a Buchwald–Hartwig-type cross-coupling with 2-(trimethylsilyl)ethane-thiol to introduce the protected thiol group.

2.2 | Synthesis and Characterization

2.2.1 | *Preparation of the Functionalized 9,9′-SBF*

The functionalization of the 9,9′-SBF moiety is shown in Scheme 2. A twofold electrophilic iodination of commercially available 2,2′-dibromo-9,9′-SBF (**5**) using PIFA and I_2 afforded 2,2′-dibromo-7,7′-diiodo-9,9′-SBF (**6**) in a yield of 81% after recrystallization from 1,4-dioxane. 2-(Trimethylsilyl)-ethanethiol was introduced in a Buchwald–Hartwig-type cross-coupling, following a modified literature procedure [45] to provide the functionalized SBF **4** in an isolated yield of 66%. An elevated temperature of 50 °C was required for the transformation, mainly to overcome the limited solubility of compound **6**. Introduction of the 2-trimethylsilyl-ethanethiol led to a pronounced change in polarity which improved solubility and facilitated purification by flash column chromatography.

2.2.2 | *Macrocyclization*

The synthesis of the molecular loop **1** is shown in Scheme 3. The [6]CPP precursor **3** was synthesized according to an adapted literature procedure [44]. Macrocyclization was carried out under similar conditions as reported by Jasti and coworkers [35], affording macrocycle **2** in a yield of 19%. Attempts to further improve the yield by dilution of the reaction mixture and/or increasing catalyst loadings were made to suppress competing side reactions, but no significant improvements were observed. Analytical pure samples were achieved through extensive purification by flash column chromatography followed by gel permeation chromatography (GPC).

With the macrocycle **2** in hand, reductive aromatization was pursued utilizing the established $SnCl_2$/HCl system [42]. The transformation proceeded smoothly and furnished **7** in a yield of 69%. Notably, no 1,2-aryl migration or decomposition of the ethyl-TMS protecting group was observed, even under excess of $SnCl_2$/HCl at 0 °C. In a final step, transprotection of the protected sulfur groups was carried out. Full deprotection of the ethyl-TMS groups required a large excess (>20 eq.) of tetrabutylammonium fluoride (TBAF), followed by exposure to an excess of acetyl chloride that furnished the fully transprotected molecular loop **1** in a yield of 52% (Scheme 3).

2.3 | Structural Analysis

The structures of the macrocycles **2**, **7**, and **1** were confirmed by 1D and 2D NMR spectroscopy and further corroborated by high-resolution mass spectrometry (HRMS). Detailed synthetic procedures and spectroscopical data are provided in the Supporting Information (Figures S27–S42 and S57–S59). Attempts to grow single crystals for X-ray diffraction analysis failed. Despite wide range of applied conditions, crystal growth yielded exclusively bunches of fine needles lacking the required thickness for X-ray crystallography. Given that the geometry of the target structure

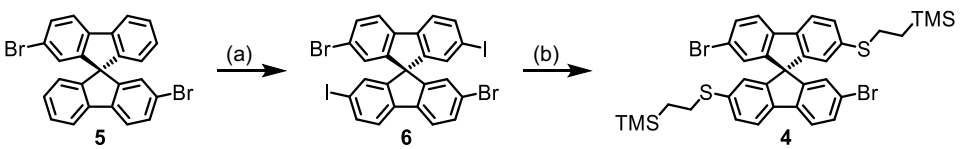

SCHEME 2 | Conditions: (a) PIFA, I_2, $CHCl_3$, 25 °C, 18 h, 81%; (b) 2-trimethylsilylethanethiol, DIPEA, $Pd_2(dba)_3$, Xantphos, 1,4-dioxane, 50 °C, 18 h, 66%.

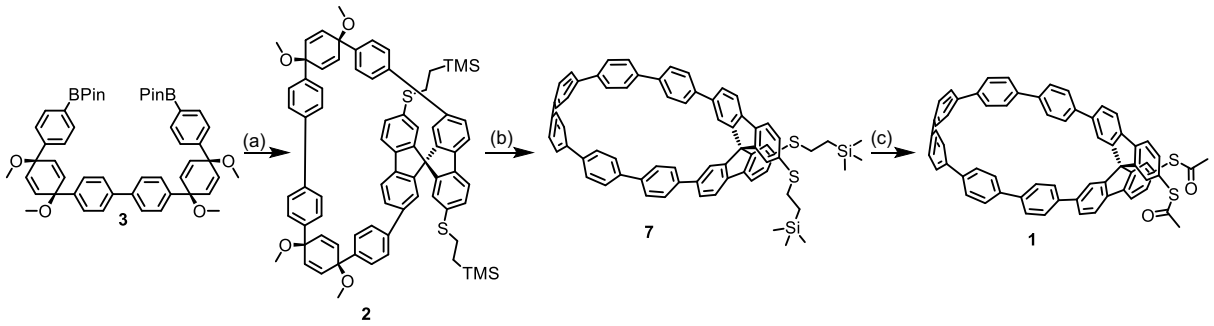

SCHEME 3 | Macrocyclization and reductive aromatization. Conditions: (a) **5**, Sphos Pd G3, K_3PO_4, 1,4-dioxane, 50 °C, 5 h, 19%; (b) conc. HCl, $SnCl_2{\cdot}2H_2O$, THF, 0 °C, 2 h, 69%; (c) (1) TBAF, THF, 25 °C, 1 h. (2) AcCl, THF, 25 °C, 1 h, 52%.

is also of interest for its arrangement in the junction, its optimization by density functional theory (DFT) calculation (B3LYP/def2-TZVPP; Figure 2) was considered as an alternative analysis. The loop **1** adopts a drop-like arrangement with C_2 symmetry. The central SBF motif enforces a nearly orthogonal angle of 94°, slightly larger than the 86° observed in Jasti's figure-eight macrocycle [35], likely due to the reduced steric hindrance of the flexible S-acetyl groups. The internal cavity spans approximately 9.1 Å across and 13.3 Å from top to bottom, consistent with the dimensions reported for the figure-eight macrocycle. As a consequence of this geometry, the strain is not evenly distributed across the phenylene backbone. The boat angle increases from 3.7° from the SBF core to 15° at the outer turning point of the CPP segment. The mean torsion angles between the phenylene units were determined to be 28.1°, 35.9°, 26.6°, and 26.8°, starting from the SBF core. These values are in the range of commonly observed values for strained CPP system [35] but show local variation due to the macrocycle's asymmetry.

To evaluate the spiroconjugative interaction across the central spiro node, the frontier molecular orbitals (MOs) of macrocycle **1** obtained from DFT calculations were analyzed. The HOMO and HOMO-1 exhibit the characteristic spiro-splitting into spiro-antibonding and spiro-bonding respectively, arising from the interaction of the four *p*-orbitals adjacent to the central spiro atom (Figure S18) [46–49]. The calculated energy difference of $\Delta E = 0.358$ eV provides a quantitative description of the spiroconjugative interaction within the macrocycle. For comparison, unsubstituted 9,9′-SBF was optimized at the same level of theory. The corresponding spiro-bonding/spiro-antibonding orbital pair exhibits an energy gap of $\Delta E = 0.267$ eV, compared to the 0.358 eV of macrocycle **1**. Although both orbitals are delocalized over the CPP backbone, the phase relationships around the spiro center demonstrates electronic communication between the two orthogonal fluorene π-systems supporting the presence of a spiroconjugated pathway for charge transport.

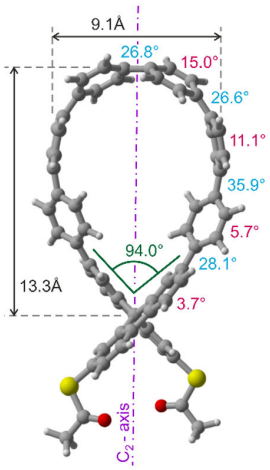

FIGURE 2 | Structural analysis of **1**. Molecular dimensions (black), mean phenylene torsion angle (blue), and boat angle of each phenylene (red).

2.4 | Optical Analysis

The absorption spectra of the macrocyclic loops **2**, **7**, and **1** were recorded in CH_2Cl_2 at room temperature (Figure 3a). Macrocycle **2** (Figure 3, green trace), the nonaromatized precursor, exhibits an absorption maximum at 338 nm with an extinction coefficient of $9.69 \times 10^4\,M^{-1}cm^{-1}$. Local maxima in the range of 250–270 nm are attributed to transitions of the cyclohexadiene units [50] while the band at 338 nm originates from the SBF moiety [32]. Upon reductive aromatization, the resulting loop-type macrocycles **1** (Figure 3, orange trace) and **7** (Figure 3, purple trace) show a distinct bathochromic shift with absorption maxima at 343 and 349 nm respectively, with a trailing shoulder at around 400 nm. These values are slightly redshifted compared to the reported values for [*n*]CPP series ($\lambda_{max} = 335$–340 nm) [51] suggesting an extension of the π-conjugated system. The extinction coefficients are notably high, reaching up to $1.43 \times 10^5\,M^{-1}cm^{-1}$ for **1** and $1.14 \times 10^5\,M^{-1}cm^{-1}$ for **7**. These values are comparable to those of [10]CPPs ($\varepsilon = 1.3 \times 10^5\,M^{-1}cm^{-1}$) [51] and approximately half that for the corresponding reported figure-eight [35]. This enhancement in absorptivity and redshifted character reflects the increased delocalization and symmetry present in the aromatized systems.

To support the experimental assignments, TD-DFT calculations were performed for macrocycle **1** at B3LYP/def2-TZVPP level of theory. The simulated absorption spectrum is in good agreement with the experimental data (Figure S15), reproducing the main absorption bands. The major contribution to the band at 349 nm arises from transitions S_2, S_3, and S_6 which involve a combination of transitions from highest occupied molecular orbital (HOMO) – 2 to lowest unoccupied molecule orbital (LUMO) + 1. The weaker shoulder observed around 400 nm is

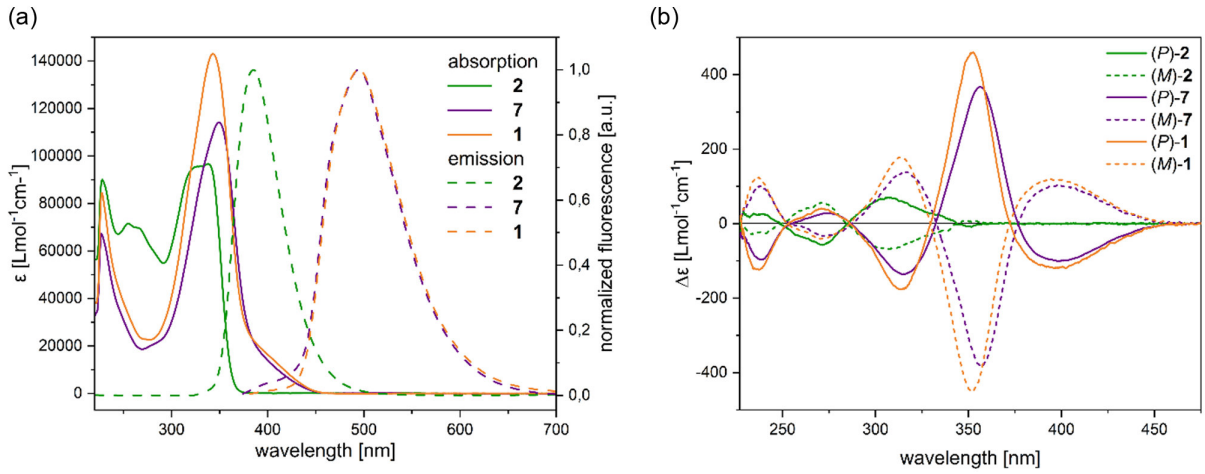

FIGURE 3 | (a) Absorption and emission of compounds **1**, **2**, and **7** recorded in CH_2Cl_2 at 25 °C. (b) ECD spectra of the enantiomers **1**, **2**, and **7** recorded in CH_2Cl_2 at 25 °C.

also reproduced and corresponds to the lowest energy transition (S_1) which can be assigned to the HOMO–LUMO transition. The oscillator strengths indicate that the transitions S_2, S_3, and S_6 are consistent with the observed high intensity of the experimental band at 349 nm, supporting their assignment as the primary π–π* transitions delocalized across the macrocycle. With S_1 being the lowest energy excited state, it is expected to be the origin of the fluorescence emission. The macrocyclic loops **1** and **7** both display a single-emission band at 494 nm, in line with the emission maxima of [9]CPP (λ_{em} = 494 nm) [51]. In contrast, the fluorescence of the nonaromatized precursor **2** is blueshifted by approximately 100 nm and appears at 385 nm (Figure 3a). All three macrocycles exhibit high fluorescence quantum yields (Φ_f) in the range of 53%–56% upon excitation at 340 nm (Table 1).

2.5 | Chirality and Optical Activity

Enantiomeric separation of the racemic macrocyclic loops **1**, **2**, and **7** was carried out on preparative scale using chiral stationary-phase high-performance liquid chromatography (HPLC) (Figure S7–S9). The separated enantiomers are mirror images and exhibit Cotton bands of opposing signs, confirming the inherent chirality of the molecular wire (Figure 3b). The CD signals corroborate the absorption bands observed in the UV–vis spectrum, further indicating that the optical activity arises from symmetry-allowed π–π* transitions of the conjugated backbone. The simulated CD spectra (Figure S14), obtained from TD–DFT calculations reproduced the experimentally observed Cotton bands of (*M*)-**1**, enabling assignment of the first-eluting enantiomer as (*P*)-**1** and the second as (*M*)-**1**. The enantiomeric assignment of macrocycles **2** and **7** was achieved through enantiopure synthesis (see Supporting Information pages 21–22). With the absolute configurations established, the chiroptical properties of the three macrocycles were compared by evaluating their molar circular dichroism ($\Delta\varepsilon$) and dissymmetry factors (g_{abs}). A notable difference is observed between the CD signals of the fully aromatized macrocycles **1** and **7** and those of the precursor **2**. Prior to reductive aromatization, macrocycle **2** exhibits three Cotton bands with the most intense and redshifted signal appearing at 307 nm ($\Delta\varepsilon = 70.2\,L\,mol^{-1}cm^{-1}$) and displays a dissymmetry factor (g_{abs}) of 1.0×10^{-3} at 302 nm (Figure 3b, green spectra). These Cotton bands are primarily attributed to the 9,9′-SBF core as previously reported in literature [52, 53]. In comparison, the CPP-containing macrocycles **1** and **7** show a distinct increase in molar circular dichroism ($\Delta\varepsilon$), by a factor of approximately six (Table 1). The most intense Cotton bands are redshifted to 352 and 357 nm respectively, followed by a broad Cotton band around 400 nm, consistent with earlier reports on chiral CPP-based macrocycles [54]. Correspondingly, the g_{abs} values increase to $7.0–8.4\times10^{-3}$ (Table 1). Interestingly, the three Cotton bands attributed to the SBF core in macrocycle **2** are also observed in **1** and **7**, albeit with increased intensity. However, the sequence of the Cotton bands signs is inverted. The (*P*)-**2** enantiomer shows an overall CD pattern of (+/−/+), whereas the same pattern appears in (*M*)-**7** and (*M*)-**1**. This inversion indicates a change in the coupling of electronic transitions upon aromatization.

TABLE 1 | Optical properties of the macrocyclic loops 1, 2, and 7.

	λ_{abs} [a]	ε [b]	λ_{em} [a]	Φ_f	g_{abs} [b]
2	338	96.6×10^3	385	56.5% (340)	1.0×10^{-3} (302)
7	349	11.4×10^4	494	53.6% (340)	8.4×10^{-3} (415)
1	343	14.3×10^4	494	53.5% (340)	7.0×10^{-3} (416)

[a]Wavelengths in nm.
[b]Molar extinction coefficient in $M^{-1}cm^{-1}$, for the most redshifted local maxima.

2.6 | Charge Transport Studies

The molecular loop **1** was measured at room temperature and ambient pressure in a home-built mechanically controlled break-junction (MCBJ) setup [55–57]. The device uses a three-point bending stage to strain a flexible substrate bearing a lithographically patterned Au nanowire (Figure 4a). A piezoactuator modulates the strain, enabling reversible rupture and reformation of the central Au constriction and allowing acquisition of thousands of breaking traces per device. A 0.1 mM solution of the loop **1** in CH_2Cl_2 was drop cast onto the chip. Single-molecule junctions form when a molecule bridges the Au electrodes, producing a

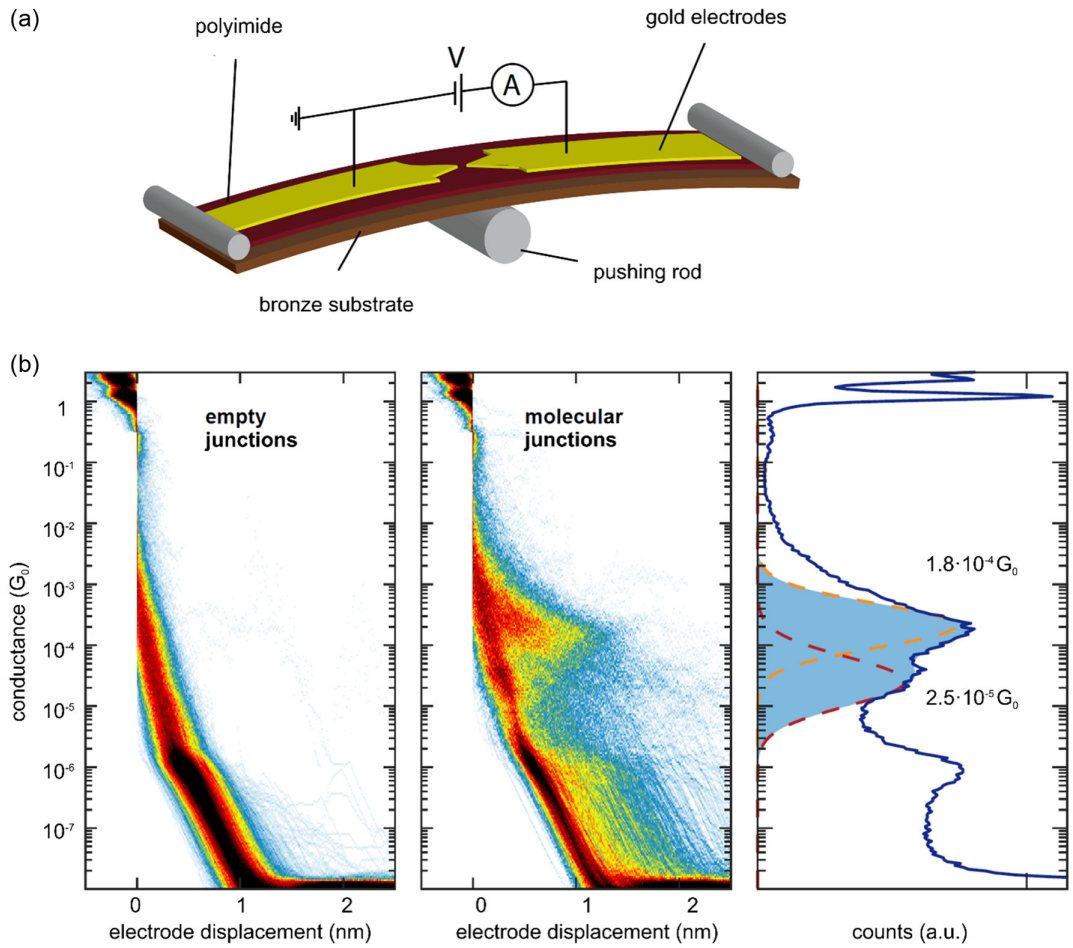

FIGURE 4 | Conductance measurements of single-molecule junctions. (a) Schematic of the MCBJ technique. (b) 2D conductance histograms of empty tunneling traces and of molecular traces separated by a trained neural network, together with the 1D conductance projection of the molecular traces ($N = 7158$ traces). Two conductance plateaus emerge at 1.8×10^{-4} G_0 and 2.5×10^{-5} G_0. The feature near 1×10^{-6} G_0 originates from the logarithmic amplifier used for current readout [56]; its characteristic bias dependence supports a nonmolecular origin [57].

plateau-like feature in the conductance versus electrode displacement curve. Two independent samples were examined at 100 mV; one was measured at 200 and 500 mV to assess bias dependence and strengthen statistics. For loop **1** at 100 mV (Figure 4b), 7158 traces were recorded. A trained neural network separated tunneling (empty) from molecular traces [58], yielding a 31.7% fraction of the latter. The 1D conductance histogram exhibits two peaks at 1.8×10^{-4} G_0 and 2.5×10^{-5} G_0 (Gaussian fits). The molecular traces were further partitioned by *k*-means++ clustering (Table 2) [59], revealing additional conductance plateaus not resolved in Figure 4b. A detailed processing workflow and a summary of results are provided in Supporting Information (Figure S20). These preliminary transport measurements demonstrate that the macrocyclic loop (**1**) forms stable single-molecule junctions with relatively high conductance and reproducible statistical signatures. The presence of several plateaus with distinct conductance values and lengths is consistent with the formation of diverse junction configurations. For each junction geometry, the measured conductance represents the total transmission through the complete molecular junction, to which all available transport pathways contribute. The plateau length reflects the displacement range over which the molecule and the Au contacts can rearrange without strongly changing the conductance. Both, the conductance value and the plateau length depend on the molecular arrangement within the junction. The present measurements are not sufficient to identify the microscopic junction configurations responsible for the observed conductance plateaus. Possible junction configurations include binding through both thiol-anchoring groups or through one thiol anchor and direct coupling to the CPP backbone. Reference compounds and transport calculations will be required to determine whether these or other junction configurations are responsible for the observed conductance features. Once the junction geometries are established, the conductance values can be used to assess the relevant transport pathways and possible interference effects. These studies are currently ongoing.

TABLE 2 | *k*-means++ clustering analysis. Average conductance of the two main molecular plateaus across voltages and samples (Figure S20 for additional details).

Plateau	Conductance, G_0	Length, nm
1	1.24×10^{-3}	0.65
2	1.86×10^{-4} 2.44×10^{-4}	0.63 1.05
3	3.28×10^{-5} 5.48×10^{-5}	0.82 1.23
4	8.58×10^{-6}	1.25

3 | Conclusion

The chiral macrocyclic molecular loop **1** combining a SBF core with a CPP segment was synthesized and fully characterized. The loop architecture enables a set of two distinct transport pathways: through-space spiroconjugation and radial π-conjugation. Suzuki–Miyaura-based macrocyclization with subsequent reductive aromatization afforded the target structure **1** in respectable yields. Structural and optical analyses, supported by DFT & TD-DFT calculations, revealed a strained, asymmetric macrocycle with distinct electronic signatures. Notably, the chiroptical properties undergo significant enhancement and sign inversion upon aromatization, indicating a reorganization of the electronic transitions and exciton coupling. Conductance measurements in a MCBJ setup demonstrated that the loop model compound forms stable single-molecule junctions with relatively high conductance and reproducible statistical signatures. The observed conductance features are consistent with multiple, reproducible junction configurations. These findings establish the molecular loop as a promising platform for further investigating charge transport in molecular architectures designed to provide multiple transport pathways. Current efforts focus on reference compounds and transport calculations to establish the microscopic junction geometries and assess the relevant transport pathways. The tunability and inherent chirality also present opportunities for the investigation of spin-selective transport phenomena.

Acknowledgments

H. S. J. v. d. Z. and M. M. acknowledge funding from the EC H2020 FET Open project grant agreement number 767187 "QuIET." The Mayor group acknowledges support by the Swiss National Science Foundation (200020_207744). M.M. acknowledges support from the 111 project (Grant No. 90002-18011002). Open Access funding provided by Universität Basel is acknowledged.

Open access publishing facilitated by Universitat Basel, as part of the Wiley - Universitat Basel agreement via the Consortium of Swiss Academic Libraries.

Funding

This work was supported by the Schweizerischer Nationalfonds zur Förderung der Wissenschaftlichen Forschung (200020_207744), H2020 Future and Emerging Technologies (767187 "QuIET"), and Higher Education Discipline Innovation Project (90002-18011002).

Conflicts of Interest

The authors declare no conflicts of interest.

Data Availability Statement

The data that support the findings of this study are available in the Supporting Information of this article.

References

1. A. Nitzan and M. A. Ratner, "Electron Transport in Molecular Wire Junctions," *Science* 300 (2003): 1384.

2. S. Fraysse, C. Coudret, and J.-P. Launay, "Synthesis and Properties of Dinuclear Complexes With a Photochromic Bridge: An Intervalence Electron Transfer Switching 'on' and 'off'," *European Journal of Inorganic Chemistry* 2000 (2000): 1581.

3. M. Irie, T. Fukaminato, T. Sasaki, N. Tamai, and T. Kawai, "A Digital Fluorescent Molecular Photoswitch," *Nature* 420 (2002): 759.

4. J. Liao, J. S. Agustsson, S. Wu, et al., "Cyclic Conductance Switching in Networks of Redox-Active Molecular Junctions," *Nano Letters* 10 (2010): 759.

5. M. Elbing, R. Ochs, M. Koentopp, et al., "A Single-Molecule Diode," *Proceedings of the National Academy of Sciences* 102 (2005): 8815.

6. E. Lörtscher, B. Gotsmann, Y. Lee, L. Yu, C. Rettner, and H. Riel, "Transport Properties of a Single-Molecule Diode," *ACS Nano* 6 (2012): 4931.

7. N. J. Geddes, J. R. Sambles, D. J. Jarvis, W. G. Parker, and D. J. Sandman, "Fabrication and Investigation of Asymmetric Current-Voltage Characteristics of a Metal/Langmuir–Blodgett Monolayer/Metal Structure," *Applied Physics Letters* 56 (1990): 1916.

8. S. van der Molen, R. Naaman, E. Scheer, et al., "Visions for a Molecular Future," *Nature Nanotechnology* 8 (2013): 385.

9. R. Asakawa, S. Yokoyama, R. Yamada, et al., "Periodically Twisted Molecular Wires Based on a Fused Unit for Efficient Intramolecular Hopping Transport," *Journal of the American Chemical Society* 146 (2024): 23529.

10. R. Huber, M. T. González, S. Wu, et al., "Electrical Conductance of Conjugated Oligomers at the Single Molecule Level," *Journal of the American Chemical Society* 130 (2008): 1080.

11. M. A. Reed, C. Zhou, C. J. Muller, T. P. Burgin, and J. M. Tour, "Conductance of a Molecular Junction," *Science* 278 (1997): 252.

12. J. G. Kushmerick, S. K. Pollack, J. C. Yang, et al., "Understanding Charge Transport in Molecular Electronics," *Annals of the New York Academy of Sciences* 2003 (1006): 277.

13. S. Y. Sayed, J. A. Fereiro, H. Yan, R. L. McCreery, and A. J. Bergren, "Charge Transport in Molecular Electronic Junctions: Compression of the Molecular Tunnel Barrier in the Strong Coupling Regime," *Proceedings of the National Academy of Sciences* 109 (2012): 11498.

14. J. G. Kushmerick, J. Lazorcik, C. H. Patterson, R. Shashidhar, D. S. Seferos, and G. C. Bazan, "Vibronic Contributions to Charge Transport Across Molecular Junctions," *Nano Letters* 4 (2004): 639.

15. L. Venkataraman, J. E. Klare, C. Nuckolls, M. S. Hybertsen, and M. L. Steigerwald, "Dependence of Single-Molecule Junction Conductance on Molecular Conformation," *Nature* 442 (2006): 904.

16. G. Sedghi, V. M. García-Suárez, L. J. Esdaile, et al., "Long-Range Electron Tunnelling in Oligo-Porphyrin Molecular Wires," *Nature Nanotech* 6 (2011): 517.

17. S. L. Heim, A. Gallego, V. Bertozzi, et al., "Design and Synthesis of Multipath Compact Cyclophanes for Quantum Interference Studies," *European Journal of Organic Chemistry* 27 (2024): e202400914.

18. K. Reznikova, C. Hsu, W. M. Schosser, et al., "Substitution Pattern Controlled Quantum Interference in [2.2]Paracyclophane-Based Single-Molecule Junctions," *Journal of the American Chemical Society* 143 (2021): 13944.

19. N. Xin, X. Li, C. Jia, et al., "Tuning Charge Transport in Aromatic-Ring Single-Molecule Junctions via Ionic-Liquid Gating," *Angewandte Chemie International Edition* 57 (2018): 14026.

20. D. Q. Andrews, G. C. Solomon, R. P. Van Duyne, and M. A. Ratner, "Single Molecule Electronics: Increasing Dynamic Range and Switching Speed Using Cross-Conjugated Species," *Journal of the American Chemical Society* 130 (2008): 17309.

21. M. L. Perrin, R. Frisenda, M. Koole, et al., "Large Negative Differential Conductance in Single-Molecule Break Junctions," *Nature Nanotech* 9 (2014): 830.

22. B. Alanazi, A. Alajmi, A. Aljobory, C. Lambert, and A. Ismael, "Tuning Quantum Interference Through Molecular Junctions Formed From Cross-Linked OPE-3 Dimers," *Journal of Materials Chemistry C* 12 (2024): 6905.

23. S. Soni, G. Ye, J. Zheng, et al., "Understanding the Role of Parallel Pathways via in-Situ Switching of Quantum Interference in Molecular Tunneling Junctions," *Angewandte Chemie* 132 (2020): 14414.

24. J. Hurtado-Gallego, R. Davidson, I. M. Grace, et al., "Quantum Interference Dependence on Molecular Configurations for Cross-Conjugated Systems in Single-Molecule Junctions," *Molecular Systems Design & Engineering* 7 (2022): 1287.

25. C. Yang, J. Cao, J.-L. Lin, H. Wu, H.-L. Zhang, and X. Guo, "Exceptional Field Effect and Negative Differential Conductance in Spiro-Conjugated Single-Molecule Junctions," *Journal of the American Chemical Society* 146 (2024): 29703.

26. H. E. Simmons and T. Fukunaga, "Spiroconjugation," *Journal of the American Chemical Society* 89 (1967): 5208.

27. T. P. I. Saragi, T. Spehr, A. Siebert, T. Fuhrmann-Lieker, and J. Salbeck, "Spiro Compounds for Organic Optoelectronics," *Chemical Reviews* 107 (2007): 1011.

28. T. Zhang, F. Wang, H.-B. Kim, et al., "Ion-Modulated Radical Doping of Spiro-OMeTAD for More Efficient and Stable Perovskite Solar Cells," *Science* 377 (2022): 495.

29. H. Chen, J. Zeng, R. Huang, et al., "An Efficient Aggregation-Enhanced Delayed Fluorescence Luminogen Created With Spiro Donors and Carbonyl Acceptor for Applications as an Emitter and Sensitizer in High-Performance Organic Light-Emitting Diodes," *Aggregate* 4 (2023): e244.

30. M. Valášek, K. Edelmann, L. Gerhard, O. Fuhr, M. Lukas, and M. Mayor, "Synthesis of Molecular Tripods Based on a Rigid 9,9′-Spirobifluorene Scaffold," *Journal of Organic Chemistry* 79 (2014): 7342.

31. L. Gerhard, K. Edelmann, J. Homberg, et al., "An Electrically Actuated Molecular Toggle Switch," *Nature Communications* 8 (2017): 1.

32. R. Nakazono and T. Amaya, "Synthesis and Chiroptical Properties of Macrocycles Composed of Chiral Spirobifluorenes Linked by π-Conjugated Spacers," *Bulletin of the Chemical Society of Japan* 98 (2025): uoaf046.

33. S. Kobayashi, R. Nakazono, R. Okada, M. P. Schramm, and T. Amaya, "Synthesis and Characterization of a Chiral Spirobifluorene Cyclic Hexamer," *Bulletin of the Chemical Society of Japan* 97 (2024): uoae098.

34. K. Nakagawa, K. Akimoto, B. Nakayasu, et al., "Synthesis and Host–Guest Chemistry of Chiral Spirobifluorene-Based Macrocycles Soluble in Basic Aqueous Solution," *Organic Letters* 25 (2023): 5969.

35. T. A. Schaub, E. A. Prantl, J. Kohn, et al., "Exploration of the Solid-State Sorption Properties of Shape-Persistent Macrocyclic Nanocarbons as Bulk Materials and Small Aggregates," *Journal of the American Chemical Society* 142 (2020): 8763.

36. Y. Segawa, P. Šenel, S. Matsuura, H. Omachi, and K. Itami, "[9]Cycloparaphenylene: Nickel-Mediated Synthesis and Crystal Structure," *Chemistry Letters* 40 (2011): 423.

37. E. Kayahara, Y. Sakamoto, T. Suzuki, and S. Yamago, "Selective Synthesis and Crystal Structure of [10]Cycloparaphenylene," *Organic Letters* 14 (2012): 3284.

38. R. Jasti, J. Bhattacharjee, J. B. Neaton, and C. R. Bertozzi, "Synthesis, Characterization, and Theory of [9]-, [12]-, and [18] Cycloparaphenylene: Carbon Nanohoop Structures," *Journal of the American Chemical Society* 130 (2008): 17646.

39. K. Chang, Q.-S. Deng, K. Song, et al., "Symmetry-Breaking in Carbon Nanohoops Enables Room-Temperature Ternary Single-Molecule Switching," *Angewandte Chemie International Edition* 65 (2026): e19695.

40. Y. Lv, J. Lin, K. Song, et al., "Single Cycloparaphenylene Molecule Devices: Achieving Large Conductance Modulation via Tuning Radial π-Conjugation," *Science Advances* 7 (2021): eabk3095.

41. W. Shi, M. Wang, L. Venkataraman, and J. D. Tovar, "Single-Molecule Conductance Through Hybrid Radially and Linearly π-Conjugated Macromolecules Reveals an Unusual Intramolecular π-Interaction," *Nano Letters* 25 (2025): 12101.

42. V. K. Patel, E. Kayahara, and S. Yamago, "Practical Synthesis of [n]Cycloparaphenylenes (n=5, 7-12) by H2SnCl4-Mediated Aromatization of 1,4-Dihydroxycyclo-2,5-Diene Precursors," *Chemistry – A European Journal* 21 (2015): 5742.

43. E. Kayahara, V. K. Patel, and S. Yamago, "Synthesis and Characterization of [5]Cycloparaphenylene," *Journal of the American Chemical Society* 136 (2014): 2284.

44. J. Wang, H. Shi, S. Wang, et al., "Tuning the (Chir)Optical Properties and Squeezing Out the Inherent Chirality in Polyphenylene-Locked Helical Carbon Nanorings," *Chemistry – A European Journal* 28 (2022): e202103828.

45. T. Itoh and T. Mase, "A General Palladium-Catalyzed Coupling of Aryl Bromides/Triflates and Thiols," *Organic Letters* 6 (2004): 4587.

46. A. Schweig, U. Eidner, D. Hellwinkel, and W. Krapp, "Spiroconjugation," *Angewandte Chemie International Edition in English* 12 (1973): 310.

47. J. Wilbuer, G. Schnakenburg, and B. Esser, "Syntheses, Structures and Optoelectronic Properties of Spiroconjugated Cyclic Ketones," *European Journal of Organic Chemistry* 2016 (2016): 2404.

48. K. Zhu, K. Kamochi, T. Kodama, M. Tobisu, and T. Amaya, "Chiral Cyclic [*n*]spirobifluorenylenes: Carbon Nanorings Consisting of Helically Arranged Quaterphenyl Rods Illustrating Partial Units of Woven Patterns," *Chemical Science* 11 (2020): 9604.

49. A. Ozcelik, D. Aranda, R. Pereira-Cameselle, et al., "ON/OFF Spiroconjugation Through Peripheral Functionalization: Impact on the Reactivity and Chiroptical Properties of Spirobifluorenes," *ChemPlusChem* 87 (2022): e202100554.

50. A. Abdulkarim, F. Hinkel, D. Jänsch, J. Freudenberg, F. E. Golling, and K. Müllen, "A New Solution to an Old Problem: Synthesis of Unsubstituted Poly(para-Phenylene)," *Journal of the American Chemical Society* 138 (2016): 16208.

51. E. R. Darzi and R. Jasti, "The Dynamic, Size-Dependent Properties of [5]–[12]cycloparaphenylenes," *Chemical Society Reviews* 44 (2015): 6401.

52. A. Ozcelik, M. de los Á. Peña-Gallego, R. Pereira-Cameselle, and J. L. Alonso-Gómez, "Design and Synthesis of Chiral Spirobifluorenes," *Chirality* 32 (2020): 464.

53. K. Zhu, K. Kamochi, T. Kodama, M. Tobisu, and T. Amaya, "Chiral Cyclic [n]spirobifluorenylenes: Carbon Nanorings Consisting of Helically Arranged Quaterphenyl Rods Illustrating Partial Units of Woven Patterns," *Chemical Science* 11 (2020): 9604.

54. L.-H. Wang, N. Hayase, H. Sugiyama, J. Nogami, H. Uekusa, and K. Tanaka, "Synthesis, Structures, and Properties of Highly Strained Cyclophenylene–Ethynylenes With Axial and Helical Chirality," *Angewandte Chemie International Edition* 59 (2020): 17951.

55. C. A. Martin, R. H. M. Smit, R. van Egmond, H. S. J. van der Zant, and J. M. van Ruitenbeek, "A Versatile Low-Temperature Setup for the Electrical Characterization of Single-Molecule Junctions," *Review of Scientific Instruments* 82 (2011): 053907.

56. L. Ornago, "Complexity of Electron Transport in Nanoscale Molecular Junctions" (PhD Thesis, Delft University of Technology, 2023).

57. S. van der Poel, "Interfering Electron Paths in Single-Molecule Junctions" (PhD Thesis, Delft University of Technology, 2025).

58. F. Van Veen, L. Ornago, H. S. J. Van Der Zant, and M. El Abbassi, "A Generalized Neural Network Approach for Separation of Molecular

Breaking Traces," *Journal of Materials Chemistry C* 11 (2023): 15564.

59. D. Cabosart, M. El Abbassi, D. Stefani, et al., "A Reference-Free Clustering Method for the Analysis of Molecular Break-Junction Measurements," *Applied Physics Letters* 114 (2019): 143102.

Supporting Information

Additional supporting information can be found online in the Supporting Information section. The synthesis procedures of all compounds with their corresponding full characterization as well as their spectra are provided in the Supporting Information. The authors have cited the references [35, 44] within the Supporting Information.